mathematics

MDPI

Article

Toward Optimal Fitting Parameters for Multi-Exponential DWI Image Analysis of the Human Kidney: A Simulation Study Comparing Different Fitting Algorithms

Jonas Jasse [1,*], Hans-Joerg Wittsack [1], Thomas Andreas Thiel [1], Romans Zukovs [2], Birte Valentin [1], Gerald Antoch [1] and Alexandra Ljimani [1]

[1] Department of Diagnostic and Interventional Radiology, Medical Faculty, University Hospital Dusseldorf, Heinrich-Heine-University Dusseldorf, 40225 Dusseldorf, Germany; alexandra.ljimani@med.uni-duesseldorf.de (A.L.)
[2] Department of Haematology, Oncology and Clinical Immunology, Medical Faculty, University Hospital Dusseldorf, Heinrich-Heine-University Dusseldorf, 40225 Dusseldorf, Germany
* Correspondence: jonas.jasse@med.uni-duesseldorf.de; Tel.: +49-211-81-18044

Abstract: In DWI, multi-exponential signal analysis can be used to determine signal underlying diffusion components. However, the approach is very complex due to the inherent low SNR, the limited number of signal decay data points, and the absence of appropriate acquisition parameters and standardized analysis methods. Within the scope of this work, different methods for multi-exponential analysis of the diffusion signal in the kidney were compared. To assess the impact of fitting parameters, a simulation was conducted comparing the free non-negative (NNLS) and rigid non-linear least square (NLLS) fitting methods. The simulation demonstrated improved accuracy for NNLS in combination with area-under-curve estimation. Furthermore, the accuracy and stability of the results were further enhanced utilizing optimized parameters, namely 350 logarithmically spaced diffusion coefficients within $[0.7, 300] \times 10^{-3}$ mm^2/s and a minimal SNR of 100. The NNLS approach shows an improvement over the rigid NLLS method. This becomes apparent not only in terms of accuracy and omitting prior knowledge, but also in better representation of renal tissue physiology. By employing the determined fitting parameters, it is expected that more stable and reliable results for diffusion imaging in the kidney can be achieved. This might enable more accurate DWI results for clinical utilization.

Keywords: diffusion-weighted MRI; multi-exponential; microstructural image analysis; simulation; fitting; modelling; kidney

MSC: 92C55; 68U10; 92C50; 11L07; 92-10

Citation: Jasse, J.; Wittsack, H.-J.; Thiel, T.A.; Zukovs, R.; Valentin, B.; Antoch, G.; Ljimani, A. Toward Optimal Fitting Parameters for Multi-Exponential DWI Image Analysis of the Human Kidney: A Simulation Study Comparing Different Fitting Algorithms. *Mathematics* **2024**, *12*, 609. https://doi.org/10.3390/math12040609

Academic Editor: Takashi Suzuki

Received: 31 January 2024
Revised: 15 February 2024
Accepted: 17 February 2024
Published: 18 February 2024

1. Introduction

Diffusion-weighted MRI (DWI) is a specialized imaging technique that offers insights into the microstructure of tissue by assessing the movement of water molecules within the tissue microstructure without the need for tracer injections [1,2]. It is widely used in clinical settings to detect, characterize, and stage malignant lesions in various anatomical regions of the human body. Furthermore, DWI distinctive ability to quantify diffusion processes can be utilized to detect and characterize fibrosis and inflammation including but not limited to the abdomen. In terms of kidney applications, it enables differentiation between healthy tissue and tissue affected by renal failure, pyelonephritis, ureteral obstruction, and renal cell carcinoma [1,3,4]. A precise description of the acquired MRI signal is crucial in order to distinguish between physiological and pathological processes.

To evaluate an acquired DWI signal, multi-exponential signal analysis can be used. The conventional Intra-Voxel Incoherent Motion (IVIM) model proposes a two-compartment

model consisting of fractions related to capillary perfusion and tissue diffusion [5]. However, recent studies have indicated that bi-exponential modelling of the diffusion signal is insufficient to describe the behavior of water molecules in complex environments such as the human kidney. The kidney is composed of various structures of varying magnitudes, including dense tissue, small capillaries, and large blood vessels. This results in different diffusion environments in the renal cortex, medulla, and hilum, thus rendering a bi-exponential description insufficient [6–11]. Instead, a more appropriate approach in renal tissue involves a tri-exponential model, which encompasses the three diffusion regimes with contributions from blood flow, tubular flow, and pure tissue diffusion [7–10].

The standard method for fitting the IVIM model to the acquired renal DWI data is to perform non-linear least squares fitting (NLLS) [12] of a predefined rigid tri-exponential model. However, NLLS requires initial estimated starting values. Starting from this initial guess, the values are varied until the tri-exponential model function best fits the measured data using least squares. That way, NLLS provides a distinct unique solution for each unknown, poorly representing physiological conditions with variable value spectrums. Because NLLS requires prior knowledge regarding the number of components, its use has been limited so far. Especially in pathophysiological conditions, initial fitting values are difficult to determine and the number of diffusion compartments may vary [13]. Therefore, the recently utilized non-negative least squares fitting (NNLS) [14] approach presents an advantage, as it does not demand further specification of underlying diffusion components or specific initial starting values a priori, making it potentially superior to the NLLS algorithm. In contrast to NLLS, which requires a specific model function—in this case a tri-exponential model—to be specified, NNLS automatically determines the number and size of the exponential terms based on a specified (pseudo) continuous spectrum of exponential functions. The only assumption made, which applies to diffusion, is that the coefficients of interest should not be negative. NNLS results in a distribution of exponential terms that directly reflects the diffusion compartments of the renal tissue being studied. Therefore, NNLS has the potential to better reflect the complex characteristics of biological tissue. Nevertheless, a systematic quantitative comparison of these different signal analysis techniques and the establishment of standardized parameters for multi-exponential renal DWI investigations is missing to date.

To identify optimized fitting parameters, this study aims to compare and evaluate the NLLS and NNLS fitting approaches using an extensive multi-parametric simulation. Firstly, a synthetic multi-exponential diffusion signal was simulated, based on physiological conditions present in the human kidney. Extensive signal analysis was then performed using the introduced fitting approaches with various parameter variations. Moreover, both NLLS and NNLS were combined by using the NNLS results as initial values for the rigid non-linear fitting method (named NLLS*). In addition, the NNLS algorithm was enhanced by incorporating an area-under-curve (AUC) function to improve accuracy, referred to as $NNLS_{AUC}$. Afterwards, we conducted a comprehensive comparison of the results obtained from all four multi-exponential fitting techniques and derived the optimal fitting parameters. These parameters were subsequently applied to a thorough final simulation.

This study aims to determine optimized acquisition and fitting parameters by conducting a comprehensive evaluation of the NLLS and NNLS fitting approaches through extensive multi-parametric simulations based on physiological conditions present in the human kidney. Therefore, we determined a set of optimized parameters that can serve as basis for accurate analysis of real renal DWI data using multi-exponential methods.

The paper is structured as follows. Section 2 describes the mathematical model and the fitting algorithms and explains the generation of the synthetic multi-exponential signal. Next, the simulation conditions are presented in the same section, showing the parameters used and further details of the parameter variations performed. The section ends with a comprehensive description of the statistics used to evaluate the results. The results are

presented in Section 3, followed by a full discussion in Section 4. Finally, Section 5 presents the conclusions of this work.

2. Methods

2.1. Multi-Compartment Model

The diffusion signal $S(b)$ observed in the human body can generally be described as a superposition of multiple individual diffusion processes, with various diffusion coefficients resulting in a multi-exponential decay function [15]:

$$S(b_i) = \sum_{i=1}^{M} f_j e^{-b_i D_j}, \;\; j = 1, 2, \ldots, N \tag{1}$$

where b_i is the diffusion weighting b-value in mm^2/s, M is the total number of measurements i with different b-values, f_j is the amplitude of the exponential component with the diffusion coefficient D_j. In the following, f_j is denoted as the volume fraction, although this nomenclature is mathematically inaccurate due to the omission of correction for relaxation times and the exclusion of the prevailing proton density. N is the number of diffusion components. Typically, mono- or bi-exponential models are used to describe DWI data from certain organs. However, recent studies have questioned the correctness of bi-exponential fitting for the diffusion signal, particularly for renal tissue [8,9,11,16]. It appears as though a three-compartment model, considering the tubular volume fraction, is physiologically more appropriate in the context of the kidney. By applying the tri-exponential fitting model, the measured diffusion signal $S(b_i)$ can be defined as:

$$S(b_i) = \sum_{i=1}^{M} f_j e^{-b_i D_j}, \;\; j \in [1, 3] \; (tissue, tubule, blood) \tag{2}$$

The diffusion coefficient D_j can be assigned to diffusion processes in tissue, tubules, and blood. In detail, these three components relate to the restricted diffusion of water molecules in renal tissue, the pseudo-diffusion occurring inside tubules, and the pseudo-diffusion component present in blood vessels. They are often referred to as the slow, intermediate, and fast diffusion components, respectively. The same classification accounts for the three different volume fractions f_j.

The sum of all volume fractions in multi-compartment models adds up to $\sum_j^N f_j = 1$. Therefore, the diffusion signal $S(b_i)$ for a three-compartment model can be defined as:

$$S(b_i) = \sum_{i=1}^{M} f_{slow} e^{-b_i D_{slow}} + f_{inter} e^{-b_i D_{inter}} + (1 - f_{slow} - f_{inter}) e^{-b_i D_{fast}} \tag{3}$$

2.2. Non-Linear Least Square Fitting

The established tri-exponential model described in Equation (3) was incorporated into a rigid NLLS algorithm constructed around the *lsqnonlin* function of MATLAB (The Mathworks Inc., Natick, MA, USA). To fit the synthetic signal (construction details provided below), the standard trust-region algorithm [17] was employed. Initial parameter values for D, f, and boundary conditions of the non-linear fit need to be declared a priori. Hence, standard starting values and parameter ranges were chosen in accordance with literature [13], as summarized in Table 1. Following the fitting process, the NLLS algorithm produced discrete optimal values for D_j and f_j with respect to the corresponding signal input.

Table 1. Ground truth values required for the generation of synthetic multi-exponential diffusion decay data and standard simulation parameters.

Ground truth values	
Diff. coefficient blood (d_{fast})	165×10^{-3} mm^2/s
Diff. coefficient tubule (d_{inter})	5.8×10^{-3} mm^2/s
Diff. coefficient tissue (d_{slow})	1×10^{-3} mm^2/s
Vol. fraction blood (f_{fast})	0.1
Vol. fraction tubule (f_{inter})	0.3
Vol. fraction tissue (f_{slow})	0.6
Standard simulation parameters	
b-value distribution [16]	[0, 5, 10, 20, 30, 40, 50, 75, 100, 150, 200, 250, 300, 400, 525, 750]
SNR	140
Iterations	1000
Standard NNLS parameters	
M	300
D_{min}	0.7×10^{-3} mm^2/s
D_{max}	300×10^{-3} mm^2/s
Standard starting values NLLS	
Diff. coefficients	[1.5, 30, 100] $\times 10^{-3}$ mm^2/s
Volume fractions	[0.50, 0.25, 0.20]

2.3. Non-Negative Least Square Algorithm

To analyze the diffusion signal with the NNLS approach, an implementation of the algorithm of Lawson and Hanson [14] was employed. Fitting of the synthetic renal DWI data was accomplished with an in-house software based on the *lsqnonneg* MATLAB R2022a function. An advanced regularization method of NNLS using cross-validation to determine the regularization factor μ was implemented based on the open-source multi-exponential decay image analysis software *AnalyzeNNLS* (2017.05.09) from Bjarnason and Mitchell [18].

In the NNLS algorithm, the signal decay is expressed as a superposition of exponentials, similar to Equation (1) [15]:

$$y_i = \sum_{j=1}^{M} A_{ij} s_j, \;\; i = 1, 2, \ldots, N \tag{4}$$

with the constraint matrix A_{ij} representing the exponentials and s_j representing the corresponding amplitudes for M logarithmically spaced diffusion coefficients at N diffusion components. An inverse of A_{ij} cannot be derived due to noise contained in the signal y_i, resulting in an ill-posed problem. The NNLS algorithm is then used to minimize the minimal least squares χ^2 misfit between the measured (or simulated) and modelled data:

$$\chi^2 = min \left[\sum_{i=1}^{N} \left| \sum_{j=1}^{M} A_{ij} s_j - y_i \right|^2 \right], \tag{5}$$

while all amplitudes are implicitly defined as non-negative, stating $s_j \geq 0$ [15].

Unlike non-linear optimization methods, the NNLS algorithm does not require a priori information or an initial guess of variables to solve Equation (4). As an output, NNLS yields amplitudes for the M exponential functions for each diffusion coefficient D_j. To obtain a more physiologically realistic representation, the least-square algorithm can be adapted to

construct a continuous spectrum. By incorporating extra constraints into the matrix A_{ij}, one is able to alter the discrete character of the basic NNLS solution. By introducing the regularization term μ, Equation (5) can be adjusted accordingly [18]:

$$\chi^2 = min\left[\sum_{i=1}^{N}\left|\sum_{j=1}^{M} A_{ij}s_j - y_i\right|^2 + \mu\sum_{j=1}^{M}|s_{j+2} - 2s_{j+1} + s_j|^2\right] \quad (6)$$

The weighting factor μ serves as a smoothing constraint that affects the curvature of the NNLS solution spectrum and ensures a robust fit, determined by cross-validation. Larger μ values result in smoother distributions, satisfying the constraints at the expense of increasing misfit. For $\mu = 0$, this formula yields the least square solution χ^2_{min} from Equation (5) [18].

The outcome of the regularized NNLS fitting entails various exponential terms, which correspond to the diffusion components identified in the signal decay curve. By plotting the associated diffusion coefficients with respect to the amplitudes, distinct peaks become evident. Individual peaks can be characterized by assessing their maximum and area under curve. This allows for the derivation of the geometric mean D and volume fraction f of the contributing exponential constituents.

2.4. Combined Non-Linear and Non-Negative LS Algorithms

A unique approach was employed by combining both NNLS and NLLS methods to create a two-level analysis of the diffusion signal to overcome the starting value limitation of NLLS and thereby increase the accuracy of the fitting results. For this purpose, the NLLS algorithm utilizes the fitting results obtained by the NNLS algorithm as initial parameters, resulting in an advanced approach referred to as NLLS*.

2.5. Advanced NNLS Algorithm with AUC Constraint

In addition to the standard NNLS algorithm, we implemented an advanced fitting algorithm called $NNLS_{AUC}$. It is based on the same fitting results as standard NNLS and incorporates an AUC constraint following fitting. This modification aims to minimize the influence of inaccurately identified peaks and noise interferences. To achieve that, the $NNLS_{AUC}$ technique applies adaptable interval boundaries based on estimated physiological compartment ranges for the three diffusion regimes. In cases where multiple peaks d_{ij} are encompassed by these intervals i, a weighting factor based on their respective volume fraction f_{ij} is applied to combine them into a single representative peak d_i according to Equations (7) and (8).

$$f_i = \sum_{j=1}^{n} f_{ij}, \qquad \forall\ intervals\ i \quad (7)$$

$$d_i = \sum_{j=1}^{n} \frac{d_{ij}f_{ij}}{f_i}, \quad \forall\ intervals\ i \quad (8)$$

This categorization of the diffusion spectrum requires prior knowledge of basic diffusion regime boundary parameters.

2.6. Simulation and Reconstruction

To simulate the underlying synthetic renal diffusion data, we followed the methodology outlined in Equation (3) and used the ground truth (gT) values presented in Table 1. The initial parameters used for the diffusion coefficients d and volume fractions f are based on the physiological conditions in the human kidney, considering the presence of three diffusion compartments [9,11,13]. Subsequently, the multi-exponential diffusion signals were superimposed with Gaussian noise for each b-value on a random basis, ensuring an authentic artificial signal decay with variable signal-to-noise ratio (SNR). The SNR was defined by dividing the signal at the first b-value with b = 0 s/mm^2 by the standard

deviation of the added noise [13,19]. For better comparison, the same simulated data were then analyzed using the different algorithms mentioned above, namely NNLS and NLLS (Figure 1). In the context of the simulation, the diffusion coefficient parameter is denoted as d in order to eliminate any potential confusion with the limits of the NNLS fitting range D_{min} or D_{max}.

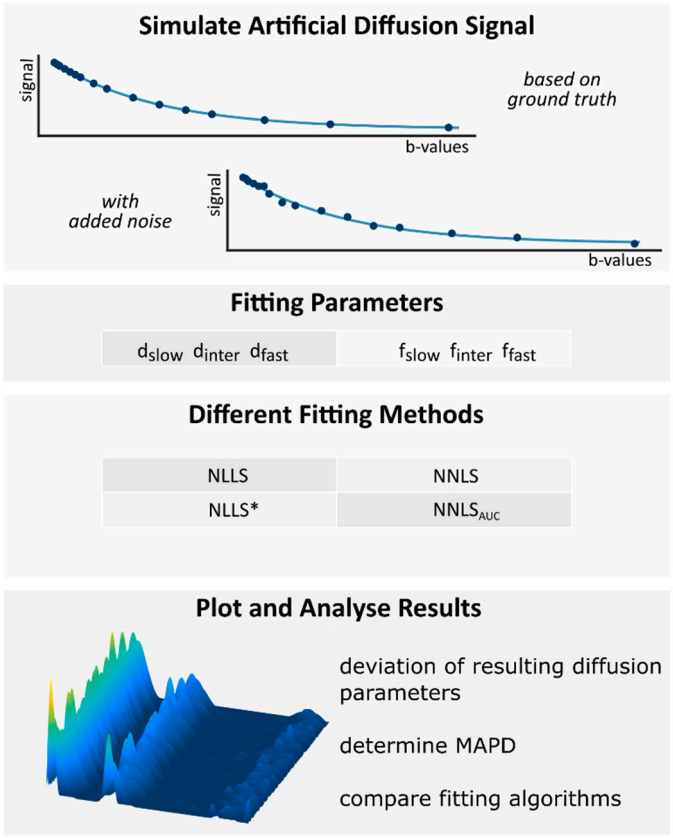

Figure 1. Simulation workflow including a list of initial parameters, the computation of synthetic signal data, the utilization of multi-exponential fitting algorithms, and the subsequent visualization and analysis of the simulation.

Values of previous works utilizing NLLS fitting were used as starting parameters [9,11,13,20,21]. The NNLS diffusion fitting range was set accordingly to encompass the entire physiologically relevant spectrum [11,13]. The total number of fitting iterations for all simulations was n = 1000.

2.7. Parameter Variation

For parameter variations, main emphasis lay on altering values within a range relevant for routine examinations of the kidneys and feasible for research imaging experiments.

The variation in SNR ranged from 50 to 600, with a primary focus on the interval between 100 and 140, including the most commonly observed SNR values of routinely acquired DWI [22,23].

In addition to the standard logarithmic distribution, other b-value compositions have been evaluated to find a suitable distribution for NNLS fitting. This work evaluates two of these other b-value compositions: an equidistant distribution and an interval distribution. The latter applies a dense concentration of b-values inside the three diffusion regimes. All b-value distributions span the same range, with b_{max} = 750.

To investigate the impact of the number of logarithmically spaced diffusion coefficients M on the NNLS fitting process, M was varied in increments of 50, resulting in a range of

100 to 600 possible exponential components for NNLS. Particular attention was devoted to the interval around M = 300, covering commonly utilized values of prior studies [11,13].

The fitting results obtained from NNLS should be self-contained from any variations made regarding the range of possible diffusion coefficients, as defined by the choice of D_{min} and D_{max}. However, altering the discrete fitting range for non-negative approaches exerts a significant influence, posing a common problem. Therefore, we compared our standard range (Table 1) to a shortened and an extended version. The shortened fitting range spans from $D_{min} = 0.9 \times 10^{-3}$ mm^2/s to $D_{max} = 200 \times 10^{-3}$ mm^2/s and the extended range encompasses values between $D_{min} = 0.5 \times 10^{-3}$ mm^2/s and $D_{max} = 500 \times 10^{-3}$ mm^2/s [11,13]. A comprehensive summary of the complete parameter variations can be found in Table 2.

Table 2. Values and sets of varied fitting parameters for NNLS.

Parameter	Variation
SNR	50, 100, 110, 120, 130, 140, 600
Equidistant b-value distribution	0, 50, 100, 150, 200, 250, 300, 350, 400, 450, 500, 550, 600, 650, 700, 750
Interval b-value distribution	0, 5, 10, 15, 20, 30, 50, 100, 150, 200, 250, 350, 450, 550, 650, 750
M	100, 200, 250, 300, 350, 400, 600
Shortened D_{min} and D_{max}	[0.8–200] $\times 10^{-3}$ mm^2/s
Extended D_{min} and D_{max}	[0.5–500] $\times 10^{-3}$ mm^2/s

2.8. Statistics

In order to compare the quality of the simulation results and depict the deviation from the gT, the Median Absolute Percentage Deviation (*MAPD*) was computed. The *MAPD* is determined by calculating the absolute difference between the parameter estimates d and f and the gT values for all $n = 1000$ iterations, expressed as a percentage:

$$MAPD(x_i) = \frac{100}{gT_i} median(|x_i - gT_i|).$$

Here x_i represents one diffusion parameter estimate and gT_i the corresponding ground truth value.

To ensure more robust results, the utilization of the median was preferred to traditional mean values. This approach bypasses the strong influence of outliers, themselves heavily biased by the choice of constraint boundaries, the latter only being applicable to NNLS algorithms [21,24].

Moreover, statistical analysis was carried out using appropriate MATLAB implementations. Visualization of the data and additional statistical measures were executed using in-house developed software in R (version 4.1.3, R Foundation for Statistical Computing, Vienna, Austria).

3. Results

3.1. Evaluation of Simulated NNLS Fitting

An exemplary NNLS analysis of $n = 100$ signals is shown in Figure 2. This simulation was performed using standard parameters (Table 1). Three distinct peaks of the slow, intermediate, and fast component can be distinguished clearly, reflecting the three diffusion compartments employed as gT for the synthetic signal decay. Additionally, minor peaks caused by wrongly interpreted noisy signal data by the NNLS algorithm are also noticeable.

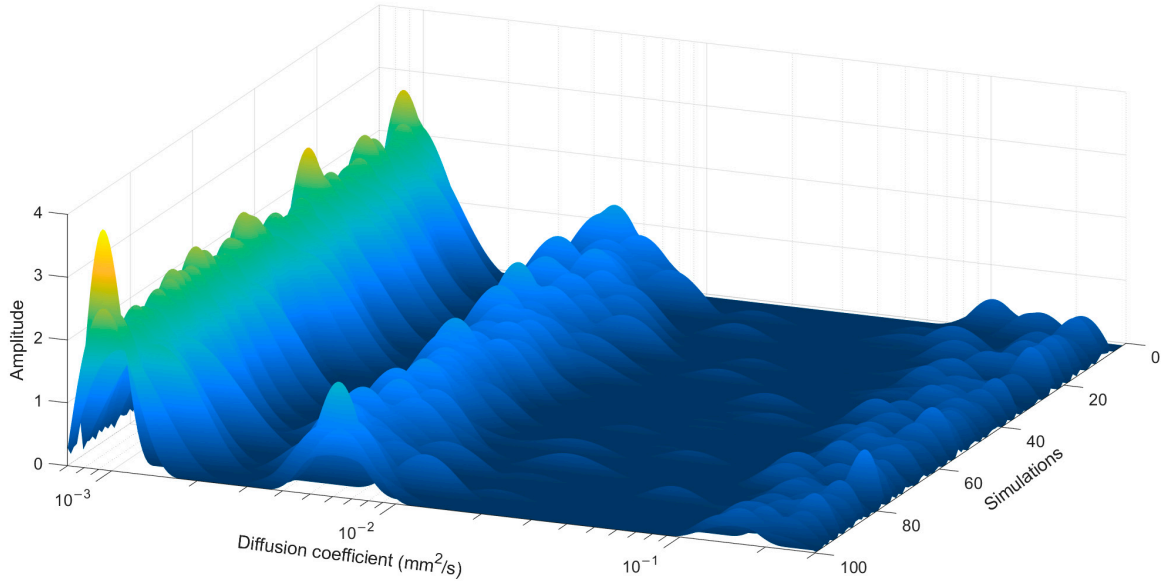

Figure 2. NNLS spectrum, representing a simulation of 100 modelled signals with an SNR of 120. Three distinctive peaks are clearly distinguishable, corresponding to the slow (**left peak**), intermediate (**middle peak**), and fast (**right peak**) components. These peaks align with the three diffusion compartments of the ground truth. Additionally, minor peaks caused by wrongly interpreted noisy signal data by the NNLS algorithm are also noticeable.

3.2. Parameter Variation

3.2.1. Signal-to-Noise Ratio

In this simulation, the SNR was varied and ranged from 50 to 600, with a primary focus on the interval between 100 and 140. The results of the simulations conducted are depicted in Figure 3A,B (for diffusion coefficients d and volume fractions f, respectively), with an optimal SNR of 600 serving as a reference. In addition to the variation in SNR, the standard simulation parameters outlined in Table 1 were employed.

The accuracy of the fitting results strongly correlates with the signal quality and, consequently, with SNR. Even in the instance of poor signal quality, with an SNR of 100 or less, differentiation of the three diffusion components remains possible with $NNLS_{AUC}$ and the standard NNLS algorithm. For the non-linear methods NLLS and NLLS*, a distinction between the slow and intermediate diffusion components can only be achieved for SNRs surpassing 130 (Figure 3). The NLLS* algorithm, up until an SNR of 600, is not capable of distinguishing the three components at any routinely achieved SNR levels.

Looking at the volume fractions (Figure 3B), the results are similar. While techniques involving non-rigid fitting possess the ability to differentiate all three compartments at SNRs of 100 and over, the results of the approaches incorporating the non-linear fitting overlap for intermediate and fast volume fractions.

In our study, NLLS methods demonstrated the highest standard derivation, particularly with respect to the slow and intermediate diffusion coefficients. Only the NNLS methods managed to distinguish all three diffusion compartments consistently.

A simplified visualization of the MAPD development with regard to increasing SNR values is illustrated in Figure A1. NLLS and NLLS* exhibit a mean MAPD of 16.46% and 18.83%, respectively. The NNLS approaches demonstrate a significantly lower average MAPD value, with plain NNLS at 12.49% and $NNLS_{AUC}$ at 10.39%. The minimum overall MAPD values concerning the routinely relevant SNR interval were observed for $NNLS_{AUC}$, reaching 9.2% at the highest SNR level of 140.

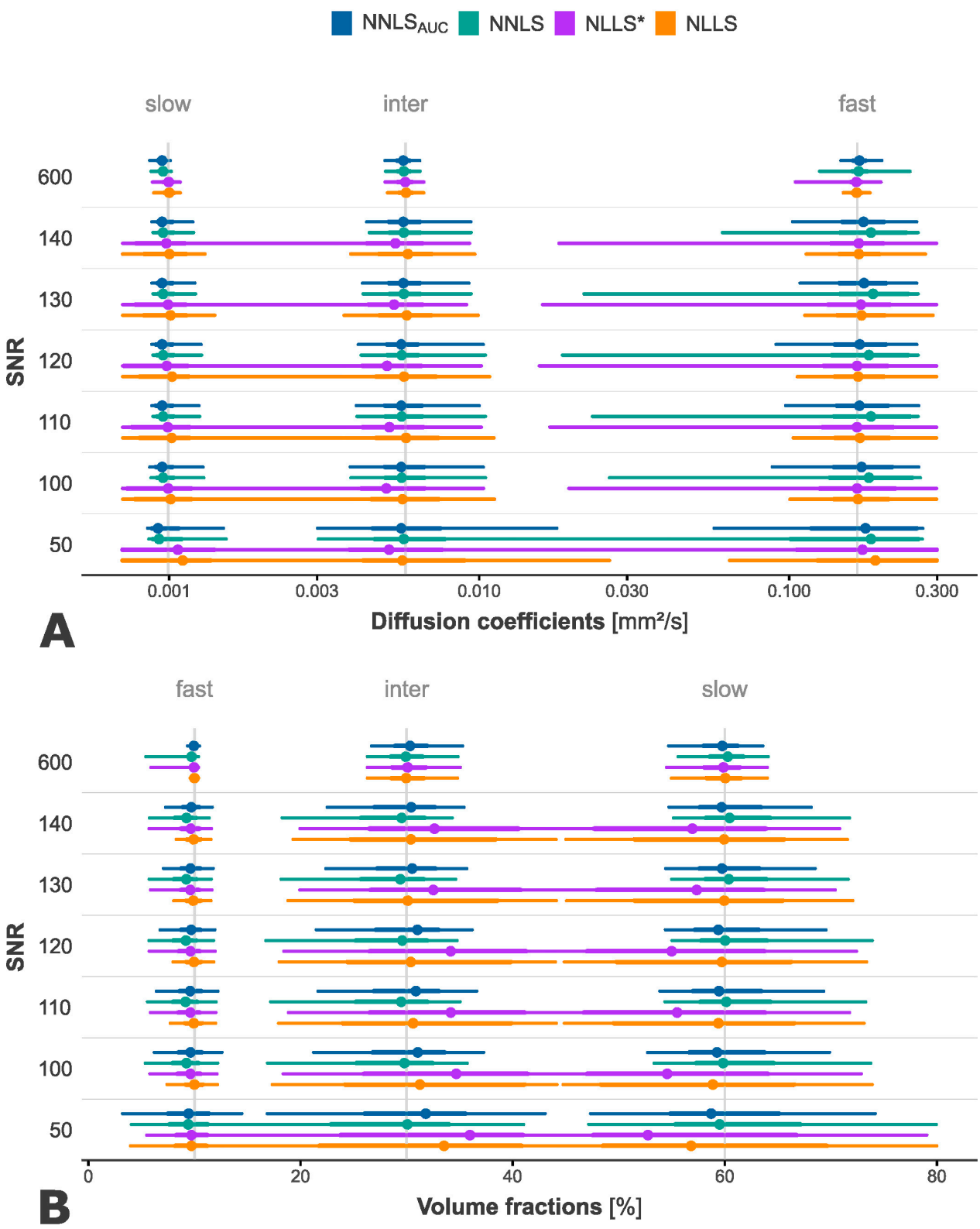

Figure 3. Simulation results for the diffusion coefficients (**A**) and volume fractions (**B**) for all SNR variations, grouped by methods. The boxplots display the median value (round dot), interquartile range (thick line), and whiskers (thin line), the latter containing 95% of the data distribution. Ground truth values are indicated by grey lines.

3.2.2. Distribution of b-Values

The evaluation of b-value distributions covers three different compositions. Figure 4 presents the findings regarding the utilized standard, equidistant, and interval distribution of b-values affecting the fitting accuracy and, consequently, the diffusion parameter estimates.

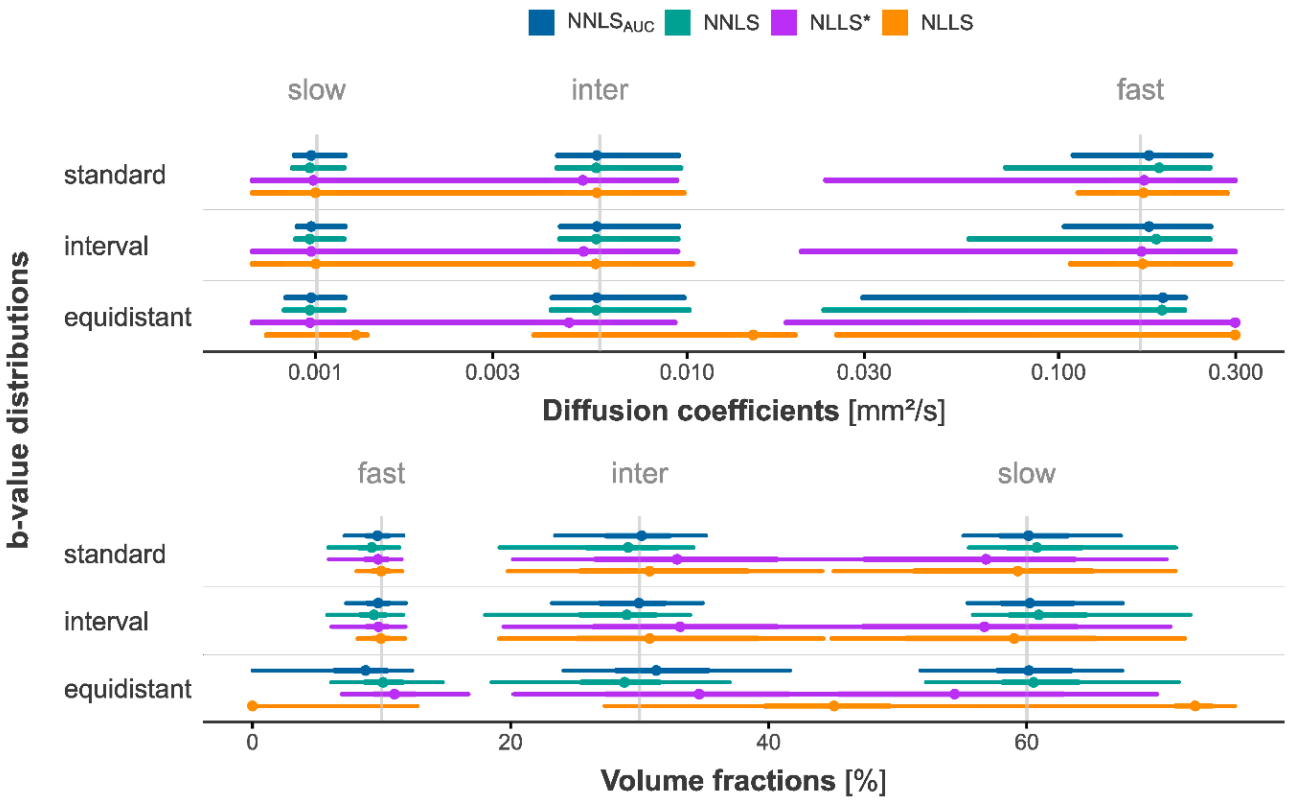

Figure 4. Simulation results of diffusion coefficients and volume fractions under variation of the b-value distribution (standard, interval, and equidistant), grouped by methods. The boxplots display the median value (round dot), interquartile range (thick line), and whiskers (thin line), the latter containing 95% of the data distribution.

A noticeable decline in accuracy can be observed when employing an equidistant distribution of b-values. Greater deviation from the gT values (12.37% mean MAPD for NNLS) across all components becomes apparent when compared to the standard distribution. However, the same is not necessarily true for the b-value composition that prioritizes the diffusion intervals. In this case, the mean MAPD for NNLS is 8.80%, slightly underperforming the standard distribution. The standard distribution, on the other hand, demonstrates the most precise results, with an average MAPD of 8.56%. In particular, the non-linear methods seem to be strongly affected by variation in the b-value distributions. In contrast, the NNLS methods exhibit more consistent results across b-value compositions.

3.2.3. Number of Logarithmically Spaced Diffusion Coefficients

For this simulation, the number of logarithmically spaced diffusion coefficients M was varied in increments of 50, resulting in a range of 100 to 600 possible exponential components for the free NNLS fitting methods. When modifying the logarithmically spaced diffusion coefficients, only NNLS and NNLS$_{AUC}$ are influenced by varying M values. Results for the diffusion coefficients are illustrated in Figure 5.

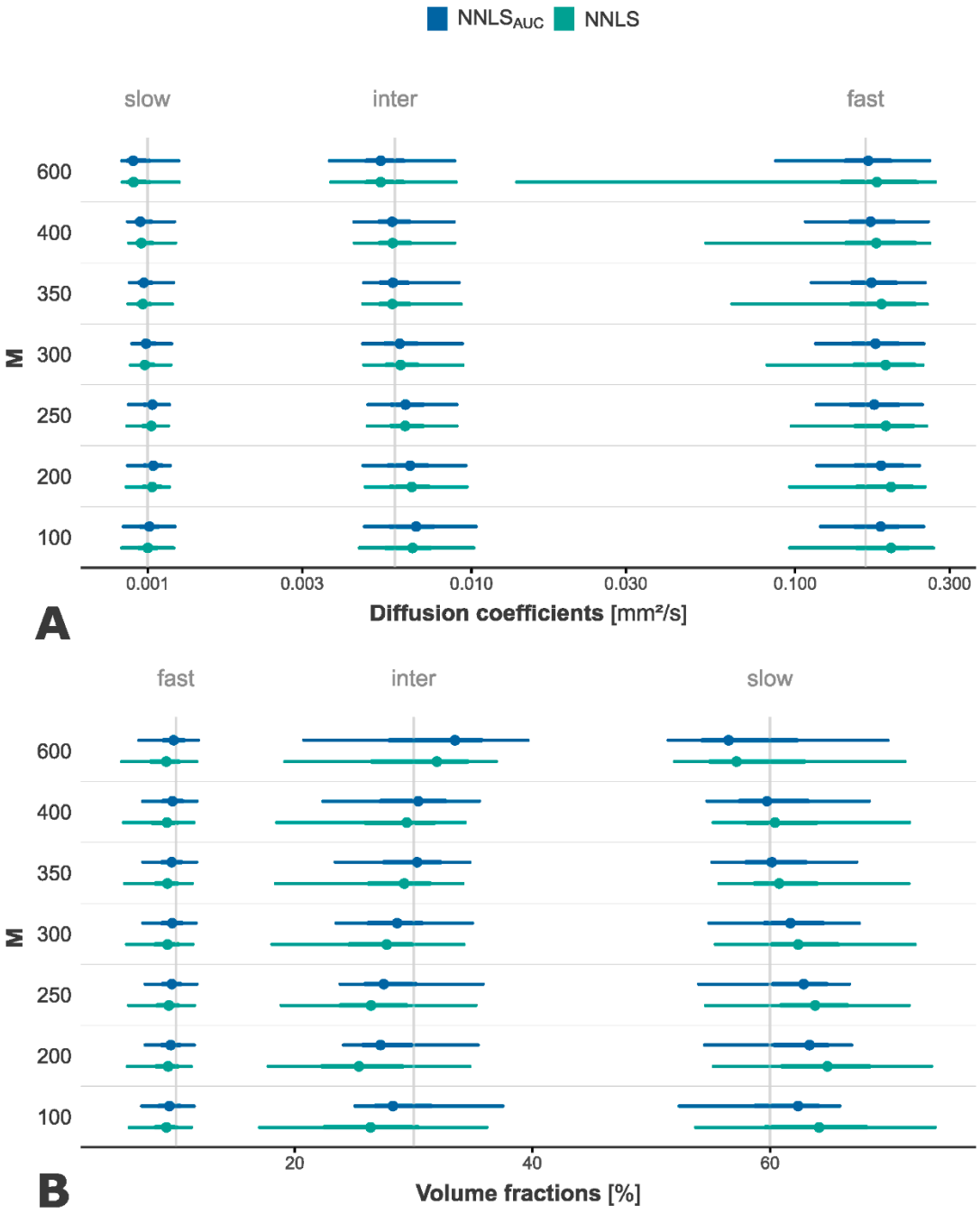

Figure 5. Simulation results for the diffusion coefficients (**A**) and volume fractions (**B**) for all variations of M, grouped by methods. The design of the boxplots is analogous to the one in prior variation figures.

Both free fitting approaches are able to distinguish the three compartments at all levels of *M*. While altering *M* only slightly affects the deviation of the results for the diffusion coefficients, it comes along with an increase in the standard derivation of the estimates for the fast component, especially in the case of NNLS. Considering f, the standard derivation remains constant, but the estimates for the intermediate and fast component vary in their derivation to the *gT*. The most accurate results are achieved when *M* is approximately 350 for NNLS and NNLS$_{AUC}$. Data for different numbers of logarithmically spaced diffusion coefficients are demonstrated in Figure A2.

The value of 350 logarithmically spaced diffusion coefficients seems most promising, with minimal deviation for both NNLS and NNLS$_{AUC}$. At $M = 350$, the total MAPD for the standard NNLS algorithm is 10.41%, decreasing to 8.36% for NNLS$_{AUC}$.

3.2.4. Diffusion Fitting Range

To investigate the impact of altering the discrete fitting range for non-negative approaches, different ranges were applied for the NNLS algorithm, namely a standard ([0.7–300] $\times$ 10^{-3} mm^2/s), a shortened ([0.9–200] $\times$ 10^{-3} mm^2/s), and an extended ([0.5–500] $\times$ 10^{-3} mm^2/s) range, as shown in Figure 6.

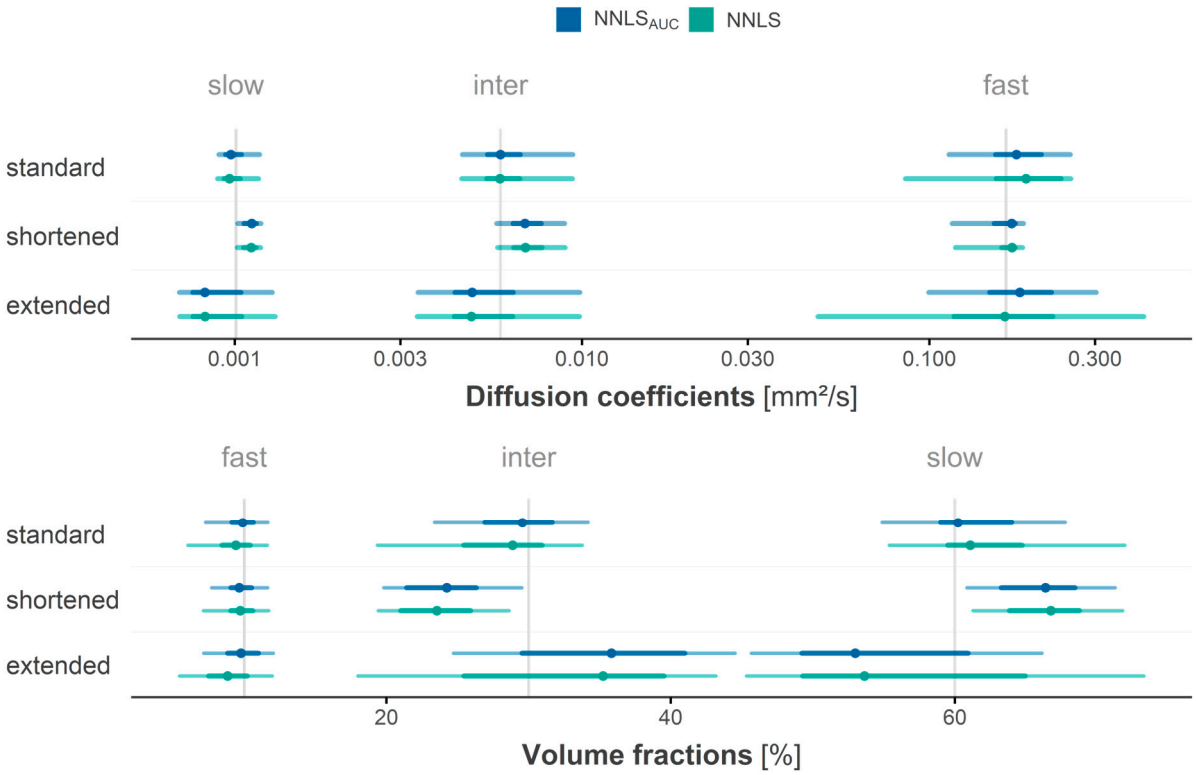

Figure 6. Simulation results of diffusion coefficients and volume fractions under variations of the diffusion fitting range, grouped by methods.

Previously used standard values for D_{min} and D_{max} produce the most accurate results, while the estimates of the shortened and extended fitting ranges deviate from the gT values. $NNLS_{AUC}$ surpasses the standard NNLS algorithm for all fitting ranges, with its total MAPD for the standard range being 8.4%. The shortened and extended ranges result in 12.31% and 18.32% deviation, respectively. The MAPD stats for standard NNLS exhibit the same tendencies but with lower accuracy.

3.3. Simulation with Optimal Simulation Parameters

For this simulation, a total of 1000 iterations were performed using the optimal parameters that have been previously evaluated. Consequently, an SNR of 140 was employed, the number of logarithmically spaced diffusion coefficients M was set to 350, and the diffusion fitting range was chosen based on the standard distribution (Table 2).

Alongside the plain NNLS algorithm, the results from $NNLS_{AUC}$, NLLS*, and standard NLLS algorithms are presented in Figure 7. The distributions of fitted values for d and f are represented by half-violin plots, while the minimalistic boxplots underneath specify the scattering by providing a visual depiction of the interquartile range (with whiskers indicated as lines and a gap in the line representing the interquartile range) and median values. The three peaks observed along the diffusion coefficient and volume fraction axis correspond to the three diffusion decay components present in the synthetic DWI signal for d and f, respectively.

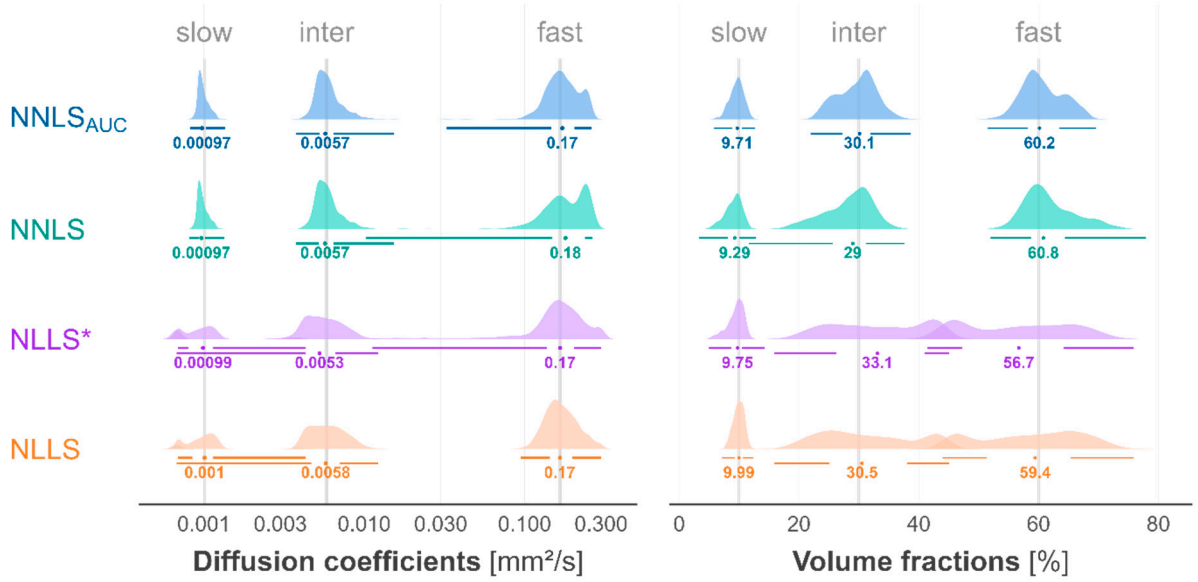

Figure 7. Simulation results of d and f grouped by methods and assigned to corresponding diffusion compartments with n = 1000 iterations. Ground truth values are indicated by grey lines. In addition to the half-violin plots representing the distribution of fitted d and f values, the minimalistic boxplots underneath specify the scattering by visualizing the associated quartile ranges and indicating the median values.

Table A1 shows the MAPD values for a simulation conducted using the previously mentioned starting values. With an average MAPD of just 10.9% for the diffusion coefficients d and 6.4% for volume fractions f, NNLS$_{AUC}$ proved to be the most accurate method with respect to gT values. Conversely, the fitting algorithms based on non-linear fitting produced the highest deviation, with an average MAPD of 16.5% and 19.2% for d along with 12.4% and 14.1% for f, in the case of NLLS and NLLS*, respectively. NNLS pre-fitting did not yield any benefits when considering the MAPD. Consequently, the results from NLLS* underperform when compared to those of the standard NLLS algorithm. As seen before, the non-linear methods encounter difficulties in differentiating the intermediate and slow components. This is evident in the significant overlaps between NLLS and NLLS*, particularly when analyzing the distribution plots. Notably, both rigid non-linear methods poorly fit the intermediate diffusion component, as indicated by the MAPD exceeding 20% for both the diffusion component and the volume fraction. For NNLS-based evaluations, on the other hand, the fast component poses the most challenges, with the highest MAPD within each parameter group reaching 25 for standard NNLS. Remarkably, NNLS$_{AUC}$ was the only method to achieve a total average deviation of less than 10%.

4. Discussion

4.1. Parameter Variations

In the present study, the NLLS and NNLS multi-exponential fitting methods were evaluated in multi-parametric simulations utilizing synthetic renal diffusion signal data. Advanced fitting algorithms based on NLLS and NNLS were implemented, and several fitting parameters were varied in order to identify the optimal parameter sets to attain the highest accuracy for the description of the renal DWI signal decay.

In existing studies, the extent of a sufficient SNR value has already been analyzed by varying the SNR with different magnitudes [13,25]. It has been found that an SNR of at least 100 is required in order to obtain reliable diffusion parameter estimates [25]. Nevertheless, a comprehensive exploration of the range of expected SNR values for in vivo DWI images is still absent. This study specifically emphasized SNR values common for DWI. As expected, a higher SNR generally results in higher output accuracy for all approaches. The NNLS

algorithms, particularly the advanced $NNLS_{AUC}$, provided more consistent results when applied to low SNR signal data. The non-linear fitting techniques exhibited limitations at SNR values below 130 and encountered difficulties with respect to the distinction of all three compartments, a phenomenon which might be due to the lack of optimal starting values for NLLS fitting. Optimization of the starting values for NLLS could improve the fitting outcomes, but this would require extensive prior work to determine the optimal parameters for individual patients, rendering it impractical for in vivo applications. NNLS methods also demonstrated less derivation at all SNR levels and proved to be the superior fitting algorithm for the SNR interval commonly encountered in routine practice.

Despite the effort to standardize DWI imaging in the kidney [26], an optimal distribution of b-values has not been established yet. Focusing on the commonly used and widely accepted b-value range of 0 to 750 s/mm^2, and considering the limitations of scan time in clinical routine, a set of 16 b-values were employed based on the findings of previous studies [10,11,13,26]. This study compared multiple b-value compositions and evaluated the impact of different distributions on fitting accuracy. Considering that low b-values are crucial for a correct and stable fit [27], and that an increased number of b-values below 100 s/mm^2 has been proved to be beneficial for fitting [10], the spacing was adjusted accordingly. Variation in b-value distributions showed superior performance with respect to the standard logarithmic composition across all different fitting approaches. The non-linear methods were greatly affected by an altered arrangement of the b-values. The equidistant distribution, in particular, compromised the fitting and parameter estimation significantly. The NNLS algorithms consistently provided stable results throughout all b-value compositions. It should further be noted that the reliability of the interval distribution may be questionable in real-world scenarios where various physiological conditions or pathologies can cause the appearance, disappearance, or shifting of different diffusion regimes within the diffusion spectrum. The study confirmed that it is crucial to cover the full b-value range, with particular attention devoted to smaller values correlating with fast diffusion motions in order to adequately represent the diffusion parameters and enable accurate fitting.

Varying the number of logarithmically spaced diffusion coefficients M for fitting in NNLS has a profound impact on the estimation of fitting parameters. When M is set to low values, similar to a very low sample rate, the ability to reliably determine the most accurate estimates is compromised. However, a very high number for M also results in divergent parameters. The choice of M is driven by a compromise between computation time and accuracy. Excessively high sample rates not only result in very long computation times, but also lead to an increased number of misinterpreted peaks in the signal data (Figure 2). If many logarithmically spaced diffusion coefficients are applied, detected regularized peaks might be split into multiple peaks. In this study, the optimal range was identified to be between 300 and 400 coefficients, with 350 providing the most accurate results for NNLS fitting techniques without a significant increase in computation time. Therefore, only in vivo data with 16 b-values in the specified standard range were considered in this study.

Furthermore, the selection of the diffusion fitting range has a significant effect on the results obtained by non-negative fitting approaches. This is a common challenge encountered in the field of multi-exponential fitting. While seeking reproducible results, it is important to avoid the expansion of the fitting range to prevent distortion of the fitting estimates. This represents a challenging task when the correct diffusion parameters of the kidney tissue are not apparent before fitting. In the current study, the $NNLS_{AUC}$ approach achieved more accurate results compared to the standard NNLS method. Among the tested diffusion ranges, neither the shortened nor the expanded intervals provided any improvements over the standard range, which spans from $D_{min} = 0.7 \times 10^{-3}$ mm^2/s to $D_{max} = 300 \times 10^{-3}$ mm^2/s.

The benefits of NNLS with varying numbers of diffusion components were not explored in this study, as Periquito et al. [13] conducted a complementary simulation approach. The study extensively investigated the impact of a varying number of diffusion components caused by pathologies such as hyperfiltration, fibrosis, and cysts. In these cases, the NNLS

algorithm was found to be superior to NLLS, as it is able to detect a fourth pathological compartment and reliably distinguish different levels of fibrosis.

4.2. Comparison of Fitting Methods

By applying optimized parameters (Table 3), the differences among the evaluated fitting algorithms become more apparent. The NNLS approaches outperformed the non-linear methods, especially owing to improved accuracy and smaller variability of the results, even though NNLS was found to incorrectly identify peaks occasionally (see Figure 2), resulting in a false fourth component that introduces bias into the results. Misfitted fourth compartments also contribute to the poor performance of NLLS*. Following the NNLS pre-fit process, the NLLS fitting was unable to effectively handle four compartments when based on a model incorporating only three diffusion coefficients, resulting in significant inaccuracies in those instances. To minimize the occurrence of misidentified compartments, further optimization is required, such as enhancement of the b-value distribution and range [13] or improvement of the quality of the acquired signal. The SNR variation demonstrates that applying NNLS to high quality signals mitigates the issue of scattering, with close to none misinterpreted signals. Thus, ensuring high signal quality for in vivo imaging, either through optimized sequence parameters or an increased number of averages, is particularly advantageous for non-negative fitting. The $NNLS_{AUC}$ method partially compensates for this limitation of the standard NNLS algorithm, including its poor performance at low SNR values, by re-evaluating the misfitted fourth compartment. This weighting approach yielded optimal results in this study. The utilization of NNLS fitting algorithms appears to be the most suitable approach for analyzing in vivo renal DWI signals. Furthermore, simulation results from this study demonstrate a significant improvement in accuracy with $NNLS_{AUC}$ as a novel fitting approach, especially when dealing with noisy image data.

Table 3. Recommended parameters for non-negative fitting.

SNR	M	D_{min}	D_{max}	b-Value Distribution
140	350	0.7×10^{-3} mm^2/s	300×10^{-3} mm^2/s	[0, 5, 10, 20, 30, 40, 50, 75, 100, 150, 200, 250, 300, 400, 525, 750]

4.3. Limitations and Outlook

It is important to note that one disadvantage of NNLS is the increased computational effort it requires. Depending on the choice of M, fitting with the NNLS algorithm takes up to 2 s per iteration. In contrast, the rigid NLLS fit is approximately 100 times faster. This discrepancy may originate from the MATLAB implementation and could potentially be addressed by employing faster programming languages and advanced implementations of the fitting algorithms. Further improvement of the code through the implementation of parallelization techniques is highly desirable to improve the computation time problem.

Bi-level optimization, as used in NLLS*, offers encouraging opportunities, but it also has limitations that need to be considered. Firstly, sensitivity to initial estimates and the risk of overfitting. While using NNLS estimates as starting points can be advantageous, the final outcome of NLLS* may still be sensitive to these initial values, making reasonably good results of the NNLS fit essential. Furthermore, the second fitting step of NLLS might not be able to improve the results significantly. Combining two fitting methods can also increase the risk of overfitting, especially when the data do not necessarily require such a complex model in the first place. This can lead to misinterpretation of the results. Additional limitations encompass the consequences of the regularization applied within the NNLS algorithm. Although regularization is necessary to enhance fitting results, it comes with miscalculation and distortion of the fitting results [19]. Given the symmetric nature of the fittings and the presence of multiple global minima, the fitting results for regularized NNLS just as NLLS may be prone to spurious minima that may not always be apparent. Despite

compensation by the high number of iterations or fitted pixels, these misfitted data points can still distort the accuracy of the outcome.

DWI data are sensitive to arbitrary diffusion processes and flowing fluids, beyond the mere presence of blood. This issue poses a challenge in the event of indiscriminate adoption of simulation parameters and may impact the quality of the fit [27]. Consequently, minor parameter adjustments may be necessary to translate the results into in vivo applications. Finally, the segmentation of the diffusion intervals for AUC calculations could potentially be adapted to accommodate other scenarios, as certain studies have assumed slightly different diffusion distributions [11,25]. The mentioned limitations, particularly their application to in vivo imaging and related adaptations, should be addressed in future studies.

The scope of this work is limited to basic least-squares approaches, not covering recent advancements in the bi-exponential IVIM model analysis which may result in improvements to multi-exponential fitting [28–30]. The application of Bayesian, neural network, and deep learning methodologies could potentially increase accuracy by identifying the distinct different diffusion components, particularly in the instance of low SNR [31]. However, these approaches have not yet been successfully tested in tri-exponential modelling. Additionally, extensive data groups are required to train neural networks, presenting a challenge to the implementation of this method due to the potential significant variances in individual patients' diffusion parameters.

5. Conclusions

To conclude, this simulation study demonstrates the advantages of free NNLS algorithms for multi-exponential fitting of renal DWI data. Modelling without an inherent number of diffusion components as in NLLS enables the reliable determination of the actual underlying diffusion compartments in the investigated tissue. NNLS provides the distribution of diffusion parameters and is less prone to inaccuracies than NLLS when compared to ground truth values.

Parameter estimates obtained through the bi-level $NNLS_{AUC}$ approach, coupled with additional area-under-curve weighting, yield further improved results and exhibit the greatest agreement with the ground truth values of this study compared to other methods. Therefore, a set of standard parameters for NNLS has been identified as a recommendation to ensure a more stable fit and reliable results for microstructural analysis of renal DWI data using multi-exponential signal analysis. The optimized fitting parameters were applied in a final systematic simulation which demonstrated the advanced accuracy of NNLS. Nevertheless, further studies are required to evaluate in vivo adaptation and assess the performance of the presented method applied to the diverse diffusion properties of human kidneys. This, especially, includes its ability to distinguish physiological and pathophysiological renal tissue, as well as its accuracy in detecting additional diffusion compartments resulting from pathologies which is of great relevance to clinical application.

Author Contributions: Conceptualization, J.J. and A.L.; methodology, J.J., A.L., H.-J.W., R.Z. and B.V.; software, J.J.; validation, J.J., A.L., B.V., R.Z. and H.-J.W.; formal analysis, all; investigation, all; resources, T.A.T. and A.L.; data curation, J.J.; writing—original draft preparation, J.J.; writing—review and editing, A.L. and T.A.T.; visualization, J.J. and T.A.T.; supervision, A.L., H.-J.W. and G.A.; project administration, A.L., G.A. and J.J.; funding acquisition, A.L. All authors have read and agreed to the published version of the manuscript.

Funding: This research received no external funding.

Data Availability Statement: The dataset is available from the corresponding author upon reasonable request.

Acknowledgments: The author of this work, Jonas Jasse, received a doctoral grant from the Jürgen-Manchot-Stiftung. A.L. was supported by an internal research grant of the local Research Committee of the Medical Faculty of Heinrich-Heine-University Düsseldorf (2020-65).

Conflicts of Interest: The authors declare no conflicts of interest.

Abbreviations

AUC	Area-Under-Curve
DWI	Diffusion-weighted Imaging
gT	Ground Truth
IVIM	Intra-voxel Incoherent Motion
MAPD	Median Absolute Percentage Deviation
NLLS	Non-Linear Least-Squares
NLLS*	Approach combining both NLLS and subsequent NNLS fitting
NNLS	Non-Negative Least-Squares
$NNLS_{AUC}$	Approach adding AUC constraint after NNLS fitting
SNR	Signal-to-Noise Ratio

Appendix A

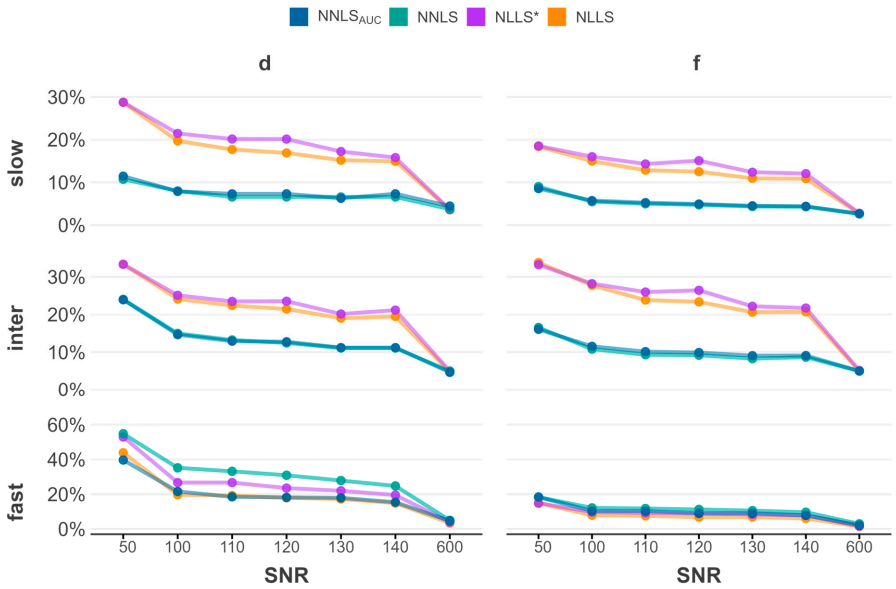

Figure A1. MAPD trend for diffusion coefficients d and volume fractions f as a function of the SNR.

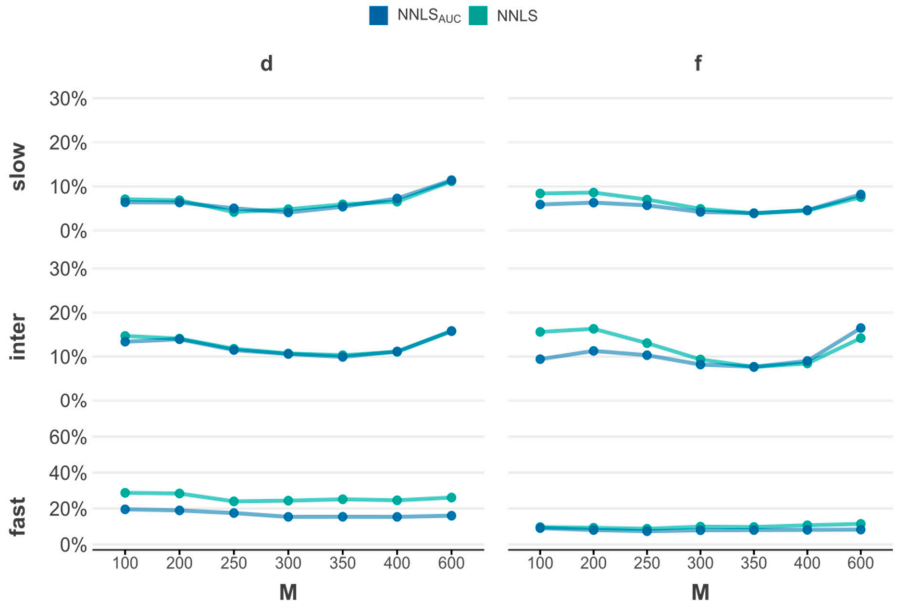

Figure A2. MAPD trend for diffusion coefficients d and volume fractions f as a function of *M*.

Table A1. MAPD for a static simulation (n = 1000) with optimal simulation parameters [in %].

Method	d_{slow}	d_{inter}	d_{fast}	Avg	f_{slow}	f_{inter}	f_{fast}	Avg	Total
$NNLS_{AUC}$	6.7	9.9	16.2	10.9	3.8	7.5	7.9	6.4	8.65
NNLS	6.4	10.3	25.0	13.9	3.9	7.6	9.9	7.1	10.50
NLLS*	15.7	22.4	19.5	19.2	12.3	22.1	8.0	14.1	16.65
NLLS	13.9	20.3	15.4	16.5	10.7	20.0	6.4	12.4	14.45

References

1. Caroli, A. Diffusion-Weighted Magnetic Resonance Imaging: Clinical Potential and Applications. *J. Clin. Med.* **2022**, *11*, 3339. [CrossRef]
2. Le Bihan, D.; Turner, R.; Douek, P.; Patronas, N. Diffusion MR imaging: Clinical applications. *AJR Am. J. Roentgenol.* **1992**, *159*, 591–599. [CrossRef] [PubMed]
3. Thoeny, H.C.; De Keyzer, F.; Oyen, R.H.; Peeters, R.R. Diffusion-weighted MR imaging of kidneys in healthy volunteers and patients with parenchymal diseases: Initial experience. *Radiology* **2005**, *235*, 911–917. [CrossRef]
4. Woo, S.; Suh, C.H.; Kim, S.Y.; Cho, J.Y.; Kim, S.H. Diagnostic Performance of DWI for Differentiating High- From Low-Grade Clear Cell Renal Cell Carcinoma: A Systematic Review and Meta-Analysis. *AJR Am. J. Roentgenol.* **2017**, *209*, W374–W381. [CrossRef] [PubMed]
5. Le Bihan, D.; Breton, E.; Lallemand, D.; Aubin, M.L.; Vignaud, J.; Laval-Jeantet, M. Separation of diffusion and perfusion in intravoxel incoherent motion MR imaging. *Radiology* **1988**, *168*, 497–505. [CrossRef] [PubMed]
6. MacKay, A.; Laule, C.; Vavasour, I.; Bjarnason, T.; Kolind, S.; Madler, B. Insights into brain microstructure from the T2 distribution. *Magn. Reson. Imaging* **2006**, *24*, 515–525. [CrossRef] [PubMed]
7. Cercueil, J.P.; Petit, J.M.; Nougaret, S.; Soyer, P.; Fohlen, A.; Pierredon-Foulongne, M.A.; Schembri, V.; Delhom, E.; Schmidt, S.; Denys, A.; et al. Intravoxel incoherent motion diffusion-weighted imaging in the liver: Comparison of mono-, bi- and tri-exponential modelling at 3.0-T. *Eur. Radiol.* **2015**, *25*, 1541–1550. [CrossRef]
8. Wurnig, M.C.; Germann, M.; Boss, A. Is there evidence for more than two diffusion components in abdominal organs?—A magnetic resonance imaging study in healthy volunteers. *NMR Biomed.* **2018**, *31*, e3852. [CrossRef]
9. van Baalen, S.; Leemans, A.; Dik, P.; Lilien, M.R.; Ten Haken, B.; Froeling, M. Intravoxel incoherent motion modeling in the kidneys: Comparison of mono-, bi-, and triexponential fit. *J. Magn. Reson. Imaging* **2017**, *46*, 228–239. [CrossRef]
10. Chevallier, O.; Wang, Y.X.J.; Guillen, K.; Pellegrinelli, J.; Cercueil, J.P.; Loffroy, R. Evidence of Tri-Exponential Decay for Liver Intravoxel Incoherent Motion MRI: A Review of Published Results and Limitations. *Diagnostics* **2021**, *11*, 379. [CrossRef]
11. Stabinska, J.; Ljimani, A.; Zollner, H.J.; Wilken, E.; Benkert, T.; Limberg, J.; Esposito, I.; Antoch, G.; Wittsack, H.J. Spectral diffusion analysis of kidney intravoxel incoherent motion MRI in healthy volunteers and patients with renal pathologies. *Magn. Reson. Med.* **2021**, *85*, 3085–3095. [CrossRef] [PubMed]
12. Marquardt, D.W. An Algorithm for Least-Squares Estimation of Nonlinear Parameters. *J. Soc. Ind. Appl. Math.* **1963**, *11*, 431–441. [CrossRef]
13. Periquito, J.; Gladytz, T.; Millward, J.; Ramos Delgado, P.; Cantow, K.; Grosenick, D.; Hummel, L.; Anger, A.; Zhao, K.; Seeliger, E.; et al. Continuous diffusion spectrum computation for diffusion-weighted magnetic resonance imaging of the kidney tubule system. *Quant. Imaging Med. Surg.* **2021**, *11*, 3098–3119. [CrossRef] [PubMed]
14. Lawson, C.L.; Hanson, R.J. *Solving Least Squares Problems*; Society for Industrial and Applied Mathematics: Philadelphia, PA, USA, 1995. [CrossRef]
15. Whittall, K.P.; MacKay, A.L. Quantitative interpretation of NMR relaxation data. *J. Magn. Reson. (1969)* **1989**, *84*, 134–152. [CrossRef]
16. van der Bel, R.; Gurney-Champion, O.J.; Froeling, M.; Stroes, E.S.G.; Nederveen, A.J.; Krediet, C.T.P. A tri-exponential model for intravoxel incoherent motion analysis of the human kidney: In silico and during pharmacological renal perfusion modulation. *Eur. J. Radiol.* **2017**, *91*, 168–174. [CrossRef]
17. Sorensen, D.C. Newton's Method with a Model Trust Region Modification. *SIAM J. Numer. Anal.* **1982**, *19*, 409–426. [CrossRef]
18. Bjarnason, T.A.; Mitchell, J.R. AnalyzeNNLS: Magnetic resonance multiexponential decay image analysis. *J. Magn. Reson.* **2010**, *206*, 200–204. [CrossRef]
19. Wiggermann, V.; Vavasour, I.M.; Kolind, S.H.; MacKay, A.L.; Helms, G.; Rauscher, A. Non-negative least squares computation for in vivo myelin mapping using simulated multi-echo spin-echo T(2) decay data. *NMR Biomed.* **2020**, *33*, e4277. [CrossRef]
20. Park, H.J.; Sung, Y.S.; Lee, S.S.; Lee, Y.; Cheong, H.; Kim, Y.J.; Lee, M.G. Intravoxel incoherent motion diffusion-weighted MRI of the abdomen: The effect of fitting algorithms on the accuracy and reliability of the parameters. *J. Magn. Reson. Imaging* **2017**, *45*, 1637–1647. [CrossRef]
21. Stabinska, J.; Zollner, H.J.; Thiel, T.A.; Wittsack, H.J.; Ljimani, A. Image downsampling expedited adaptive least-squares (IDEAL) fitting improves intravoxel incoherent motion (IVIM) analysis in the human kidney. *Magn. Reson. Med.* **2023**, *89*, 1055–1067. [CrossRef]

22. Kong, H.; Wang, C.; Gao, F.; Zhang, X.; Yang, M.; Yang, L.; Wang, X.; Zhang, J. Early assessment of acute kidney injury using targeted field of view diffusion-weighted imaging: An in vivo study. *Magn. Reson. Imaging* **2019**, *57*, 1–7. [CrossRef]
23. Zhang, G.; Sun, H.; Qian, T.; An, J.; Shi, B.; Zhou, H.; Liu, Y.; Peng, X.; Liu, Y.; Chen, L.; et al. Diffusion-weighted imaging of the kidney: Comparison between simultaneous multi-slice and integrated slice-by-slice shimming echo planar sequence. *Clin. Radiol.* **2019**, *74*, 325.e1–325.e8. [CrossRef]
24. While, P.T. A comparative simulation study of bayesian fitting approaches to intravoxel incoherent motion modeling in diffusion-weighted MRI. *Magn. Reson. Med.* **2017**, *78*, 2373–2387. [CrossRef]
25. De Luca, A.; Leemans, A.; Bertoldo, A.; Arrigoni, F.; Froeling, M. A robust deconvolution method to disentangle multiple water pools in diffusion MRI. *NMR Biomed.* **2018**, *31*, e3965. [CrossRef]
26. Ljimani, A.; Caroli, A.; Laustsen, C.; Francis, S.; Mendichovszky, I.A.; Bane, O.; Nery, F.; Sharma, K.; Pohlmann, A.; Dekkers, I.A.; et al. Consensus-based technical recommendations for clinical translation of renal diffusion-weighted MRI. *Magn. Reson. Mater. Phys. Biol. Med.* **2020**, *33*, 177–195. [CrossRef]
27. Le Bihan, D. What can we see with IVIM MRI? *Neuroimage* **2019**, *187*, 56–67. [CrossRef]
28. Gurney-Champion, O.J.; Klaassen, R.; Froeling, M.; Barbieri, S.; Stoker, J.; Engelbrecht, M.R.W.; Wilmink, J.W.; Besselink, M.G.; Bel, A.; van Laarhoven, H.W.M.; et al. Comparison of six fit algorithms for the intra-voxel incoherent motion model of diffusion-weighted magnetic resonance imaging data of pancreatic cancer patients. *PLoS ONE* **2018**, *13*, e0194590. [CrossRef] [PubMed]
29. Kaandorp, M.P.T.; Barbieri, S.; Klaassen, R.; van Laarhoven, H.W.M.; Crezee, H.; While, P.T.; Nederveen, A.J.; Gurney-Champion, O.J. Improved unsupervised physics-informed deep learning for intravoxel incoherent motion modeling and evaluation in pancreatic cancer patients. *Magn. Reson. Med.* **2021**, *86*, 2250–2265. [CrossRef] [PubMed]
30. Vidic, I.; Jerome, N.P.; Bathen, T.F.; Goa, P.E.; While, P.T. Accuracy of breast cancer lesion classification using intravoxel incoherent motion diffusion-weighted imaging is improved by the inclusion of global or local prior knowledge with bayesian methods. *J. Magn. Reson. Imaging* **2019**, *50*, 1478–1488. [CrossRef]
31. Vasylechko, S.D.; Warfield, S.K.; Afacan, O.; Kurugol, S. Self-supervised IVIM DWI parameter estimation with a physics based forward model. *Magn. Reson. Med.* **2022**, *87*, 904–914. [CrossRef] [PubMed]